SCIENCE CHINA
Information Sciences

• RESEARCH PAPER •

September 2026, Vol. 69, Iss. 9, 192501:1–192501:11
https://doi.org/10.1007/s11432-025-4760-9

Realizing scalable conditional operations through auxiliary energy levels

Sheng ZHANG[1,2,6], Peng DUAN[1,2*], Yun-Jie WANG[4], Tian-Le WANG[1,2], Peng WANG[1,2], Ren-Ze ZHAO[1,2], Xiao-Yan YANG[1,2], Ze-An ZHAO[1,2], Hai-Feng ZHANG[1,2], Zhi-Fei LI[1,2], Yuan WU[1,2], Hao-Ran TAO[5], Liang-Liang GUO[5], Lei DU[5], Chi ZHANG[5], Zhi-Long JIA[5], Wei-Cheng KONG[5], Zhao-Yun CHEN[3*], Zhuo-Zhi ZHANG[1,2,6], Xiang-Xiang SONG[1,2,6], Yu-Chun WU[1,2] & Guo-Ping GUO[1,2,5*]

[1]*Laboratory of Quantum Information, University of Science and Technology of China, Hefei 230026, China*
[2]*CAS Center For Excellence in Quantum Information and Quantum Physics, University of Science and Technology of China, Hefei 230026, China*
[3]*Institute of Artificial Intelligence, Hefei Comprehensive National Science Center, Hefei 230088, China*
[4]*Institute of the Advanced Technology, University of Science and Technology of China, Hefei 230088, China*
[5]*Origin Quantum, Hefei 230088, China*
[6]*Suzhou Institute for Advanced Research, University of Science and Technology of China, Suzhou 215123, China*

Received 30 July 2025/Revised 8 November 2025/Accepted 15 January 2026/Published online 12 August 2026

Abstract In the noisy intermediate-scale quantum (NISQ) era, flexible quantum operations are essential for advancing large-scale quantum computing, as they enable shorter circuits that mitigate decoherence and reduce gate errors. However, the complex control of quantum interactions poses significant experimental challenges that limit scalability. Here, we propose a transition composite gate scheme based on transition pathway engineering, which digitally implements conditional operations with reduced complexity by leveraging auxiliary energy levels. Experimentally, we demonstrate the controlled-unitary (CU) family and its applications. In entangled-state preparation, our CU gate reduces circuit depth by 44% for W states compared with CZ-only circuits, and this depth reduction increases the W-state fidelity by 4.20% (relative 49.27%). Furthermore, with a 72% reduction in circuit depth, we successfully implement a quantum comparator—a fundamental building block for quantum algorithms requiring conditional logic, which has remained experimentally challenging due to its inherent circuit complexity. These results demonstrate the scalability and practicality of our scheme, laying a solid foundation for the implementation of large-scale quantum algorithms in future quantum processors.

Keywords noisy intermediate-scale quantum (NISQ), conditional operations, transition composite gate, auxiliary energy levels, entangled-state preparation, quantum comparator

Citation Zhang S, Duan P, Wang Y-J, et al. Realizing scalable conditional operations through auxiliary energy levels. Sci China Inf Sci, 2026, 69(9): 192501, https://doi.org/10.1007/s11432-025-4760-9

1 Introduction

Superconducting quantum computers have progressed into noisy intermediate-scale quantum (NISQ) devices with significant potential for demonstrating quantum advantage [1–4]. However, the experimental realization of large-scale quantum algorithms is hindered by limited circuit depths due to the cumulative effects of gate errors and decoherence [3,5,6]. A pivotal strategy to overcome these challenges is developing quantum operations with enhanced operational degrees of freedom. Such advancements can effectively reduce the required circuit depth, thereby enabling the implementation of quantum algorithms on larger-scale systems [7].

The pursuit of more expressive quantum operations drives extensive research efforts. Highly expressive operations can effectively parameterize a vast and diverse set of unitary transformations, thereby providing a powerful representational capacity for approximating complex quantum processes [8,9]. These operations are primarily categorized into native and composite operations. Native operations rely on engineering novel interactions to implement flexible operations, such as arbitrary two-qubit and multi-qubit gates [10–13]. However, these approaches face challenges in multiple parameter optimization, increased system initialization overhead, and complex crosstalk corrections,

* Corresponding author (email: pengduan@ustc.edu.cn, chenzhaoyun@iai.ustc.edu.cn, gpguo@ustc.edu.cn)

thereby limiting their scalability [14–16]. By contrast, composite operations adopt a decomposition-based strategy by assembling varied gate components, with the fSim and XY-family gates serving as typical examples [9,17]. These operations often combine different two-qubit interactions or gate components through tailored pulse sequences in the time domain, effectively encapsulating them into high-expressivity gates for specific tasks. Nevertheless, these approaches increase the reliance on dynamic frequency tuning, which exacerbates frequency crowding and collision issues within large-scale quantum processors [18–21]. Alternative schemes such as block encoding can mitigate the need for dynamically tunable components by introducing auxiliary qubits, but this comes at the cost of increased hardware overhead [22–24]. Thus, while both native and composite approaches introduce more expressive gate sets at the Hamiltonian and circuit-design levels, they require careful trade-offs between interaction complexity, circuit depth, and hardware feasibility.

In this work, we propose the transition composite gate (TCG) scheme, which enables the realization of highly expressive quantum gates with reduced circuit depth. Instead of relying on auxiliary qubits, the TCG scheme temporarily exploits the intrinsic non-computational subspace of superconducting quantum systems as auxiliary energy levels. By precisely engineering the transition pathways between computational and non-computational subspaces, conditional operations are digitally constructed in a hardware-efficient manner. As a proof-of-principle demonstration, we experimentally implement a controlled-unitary (CU) operation on a superconducting quantum processor using the TCG scheme, which consists of two fixed non-adiabatic square-root controlled-phase ($\sqrt{\mathrm{CZ}}$) gates and a layer of single-qubit rotations. Quantum process tomography (QPT) validates the CU family achieved by tuning single-qubit gate parameters, with process fidelities ranging from $96.22\% \pm 0.38\%$ to $98.14\% \pm 0.39\%$ [25–27]. Furthermore, the preparation of three-qubit Greenberger-Horne-Zeilinger (GHZ) and W states demonstrates circuit depth reductions of 40.0% and 44.0%, respectively. Finally, we implement a quantum comparator—a fundamental component for conditional logic—with a significantly reduced circuit depth, showcasing the application potential of the TCG scheme [28–30]. Our work provides a hardware-efficient, high-expressivity gate construction framework for large-scale quantum computing and offers promising prospects for enhancing diverse quantum algorithms and quantum simulation.

2 Methods

2.1 Theoretical scheme

To satisfy addressing requirements, quantum units in solid-state quantum computing are typically designed with non-uniform energy level structures [31]. For example, the transmon qubit employed in this study can be treated as a qutrit [32,33], featuring an anharmonic three-level structure, as illustrated in Figure 1(a). In qubit systems, the computational subspace is spanned by the states $|0\rangle$ and $|1\rangle$ ($\mathrm{S_c}$), while state $|2\rangle$ and higher energy levels correspond to the non-computational subspace ($\mathrm{S_{uc}}$).

While the occupation of $\mathrm{S_{uc}}$ is conventionally regarded as leakage in qubit systems and is often suppressed in previous studies, it is exploited as a computational basis in qutrit-based systems [34–36]. Although ternary logic based on qutrits presents challenges regarding control complexity and algorithm compatibility, it offers novel insights for quantum gate design [37]. In particular, the temporary exploitation of $\mathrm{S_{uc}}$ facilitates the construction of conditional operations in superconducting qubit systems [38–40]. For example, non-adiabatic CZ gates accumulate controlled phases by utilizing swap-like interactions between the $|11\rangle$ and $|20\rangle$ states [41–43], a mechanism also adopted in QuAnd gates to realize multi-controlled operations [44]. More generally, fully leveraging these auxiliary states, rather than leaving them idle, enables the construction of high-expressivity gate sets. This is possible because distinct operation conditions allow for independent operations within $\mathrm{S_{uc}}$ without disturbing the states in $\mathrm{S_c}$, as illustrated in Figure 1(b). Building upon this principle, we strategically design and utilize auxiliary states as intermediate transition pathways to implement highly expressive conditional operations—a concept we refer to as the TCG scheme. Unlike conventional approaches that rely solely on decompositions confined to $\mathrm{S_c}$, the TCG scheme constructs operations across the full Hilbert space while ensuring that the final operation remains strictly confined to $\mathrm{S_c}$, with significantly reduced circuit depth compared to standard Clifford-based decompositions. This concept is analogous to the philosophy of Block Encoding [22–24], where carefully engineered gate sequences are employed to realize desired operations within the subspace of interest, with the general framework provided in Appendix A. We employ traditional Pauli gates along with the X^{12} gate between states $|1\rangle$ and $|2\rangle$, and the $\mathrm{iSWAP}_{20\leftrightarrow 11}$ gate between states $|20\rangle$ and $|11\rangle$ (also known as the $\sqrt{\mathrm{CZ}}$ gate) [44–46]. Subsection 2.2, Section 3, and Appendix B, we demonstrate several widely used controlled operations constructed from these well-established components.

It is worth noting that previous studies have indicated that utilizing high-energy levels introduces additional

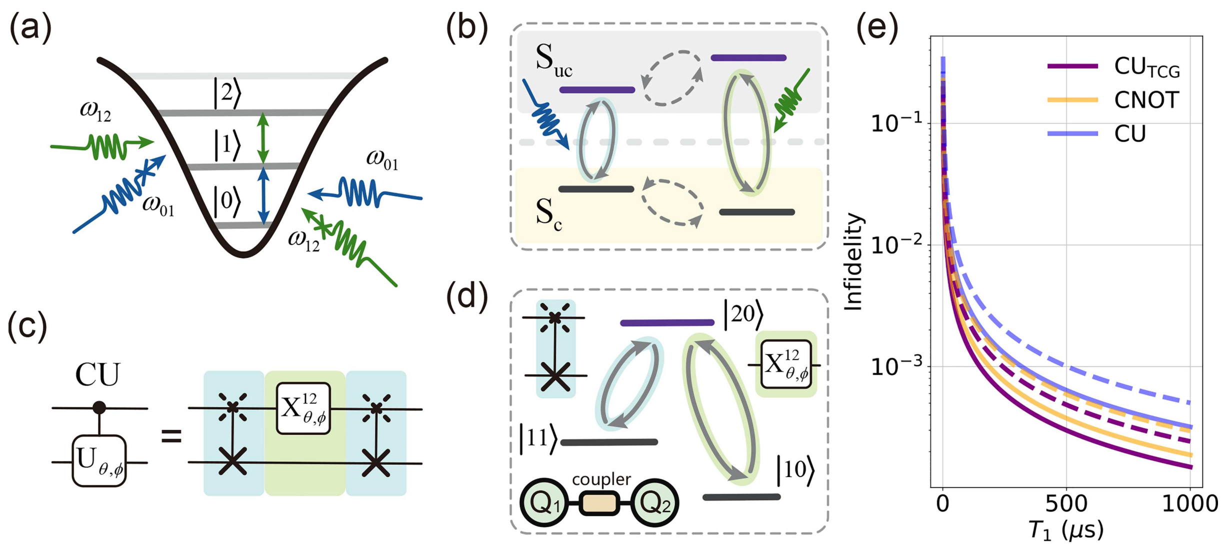

Figure 1 (a) Energy diagram of a typical transmon as a multilevel system. Microwaves of different frequencies are represented by arrows of various colors. Only those resonant with energy-level transitions induce single-qubit state transfer, rendering the effect of each drive effectively independent. Non-adiabatic two-qubit operations also give rise to distinct transition frequencies as a consequence of the non-uniform energy level structure, which enables us to treat operations in the computational subspace (S_c) and non-computational subspace (S_{uc}) independently. (b) Principle diagram of the TCG scheme. Instead of auxiliary qubits, we employ S_{uc} as auxiliary energy levels. Independent operations can be implemented within both the S_{uc} and S_c subspaces, while controlled transitions between the two subspaces are engineered as required. This allows for the reconstruction of conditional operations by deliberately transferring the quantum system into S_{uc}, utilizing its independent degrees of freedom, and subsequently returning to S_c. This procedure is referred to as transition pathway engineering. (c) Illustration of the composition of the CU gate under the TCG scheme. The X^{12} gate is applied to the high-frequency qubit to bridge the transition channel. (d) State evolution diagram corresponding to (c). The $\sqrt{\mathrm{CZ}}$ and X^{12} gates independently induce interactions between states $|11\rangle \leftrightarrow |20\rangle$ and states $|20\rangle \leftrightarrow |10\rangle$. (e) Simulated infidelity comparison among the TCG-CU gate, the CZ-based CNOT gate, and the CU gate under decoherence. Solid lines correspond to the case of $T_2 = 2T_1$, while dashed lines represent $T_2 = 0.8T_1$, which is close to the average coherence level in our system.

decoherence channels [47]. Therefore, a trade-off may be required between the occupation time of high-energy levels and the total operation duration. Additionally, the active transition into S_{uc} with imperfect control introduces a higher risk of leakage. However, these technical challenges can be addressed through continuous improvements in qubit performance and optimization of control techniques [48–50]. Therefore, in this work, we focus on verifying the feasibility of the TCG scheme and assessing its advantages in quantum circuit implementation.

2.2 Controlled-unitary gate

Flexible and efficient CU gates play a crucial role in quantum circuits [51]. However, native CU gates are constrained by complex physical implementations, while digital schemes often result in increased circuit depth. Here, the TCG scheme provides a straightforward construction of the CU gate, where an X^{12} gate is sandwiched between two $\sqrt{\mathrm{CZ}}$ gates, as illustrated in Figure 1(c). The states $|11\rangle$ and $|10\rangle$ are indirectly connected through the $\sqrt{\mathrm{CZ}}$ and X^{12} gates, with state $|20\rangle$ serving as a "bridge" for transitions effectively within S_c. Figure 1(d) illustrates the specific transition pathways of our CU operation, and the mathematical description within S_c is as follows:

$$\mathrm{CU} = \sqrt{\mathrm{CZ}} \cdot I_0 \otimes X^{12}_{\theta,\phi} \cdot \sqrt{\mathrm{CZ}} \tag{1}$$

$$= \begin{pmatrix} 1 & 0 & 0 & 0 \\ 0 & 1 & 0 & 0 \\ 0 & 0 & \cos(\frac{\theta}{2}) & -ie^{-i\phi}\sin(\frac{\theta}{2}) \\ 0 & 0 & -ie^{i\phi}\sin(\frac{\theta}{2}) & -\cos(\frac{\theta}{2}) \end{pmatrix}, \tag{2}$$

where θ and ϕ represent the Rabi angle and phase of the X^{12} gate, respectively. I_0 denotes the identity operation. In general, tunable two-qubit interactions can serve as adjustable components for implementing complex entangling operations. However, tuning these gates typically requires intricate calibration procedures involving parameters like qubit detuning and coupling strength, and often exacerbates challenges such as frequency collisions in multi-qubit architectures. In contrast, we adopt fixed-parameter two-qubit components, delegating the flexibility of gate adjustment to the X^{12} operation. As a single-qubit rotation, the X^{12} gate can be freely and precisely controlled via mature microwave techniques, with significantly lower calibration complexity. Specifically, its rotation angle θ and phase ϕ are independently and accurately determined by the amplitude and phase of the microwave drive.

The CU operation under the short-path TCG (SPTCG) scheme further reduces the required components, achieving a unidirectional state transition process. This short-path CU operation (SPCU) can be described within $\mathrm{S_c}$ as

$$\mathrm{SPCU} = I_0 \otimes \mathrm{X}^{12}_{\theta,\phi} \cdot \sqrt{\mathrm{CZ}} \tag{3}$$

$$= \begin{pmatrix} 1 & 0 & 0 & 0 \\ 0 & 1 & 0 & 0 \\ 0 & 0 & \cos(\frac{\theta}{2}) & -ie^{-i\phi}\sin(\frac{\theta}{2}) \\ 0 & 0 & 0 & 0 \end{pmatrix}. \tag{4}$$

The absence of the first $\sqrt{\mathrm{CZ}}$ operation still permits a transition from state $|10\rangle$ to $|11\rangle$, while the absence of the second $\sqrt{\mathrm{CZ}}$ operation corresponds to the reverse process. Although this omission renders the composite operation irreversible and unsuitable as a general quantum gate, it retains its capability for state preparation while reducing the overall operation duration. We provide more details in Appendix A.

In general, compared to conventional Clifford decompositions for controlled-unitary gates—which typically require two CNOT gates and three single-qubit rotations—our scheme reduces circuit depth and shortens the overall gate duration, helping to suppress error accumulation and decoherence [43, 52, 53], both of which scale with circuit complexity. We simulated the infidelity of the TCG-CU gate, the traditional CNOT gate, and the traditional CU gate under different decoherence conditions, as shown in Figure 1(e), demonstrating the advantages of our scheme. Moreover, our approach circumvents two major challenges in existing schemes. First, it avoids the hardware complexity and calibration overhead associated with direct multi-qubit interactions. Second, it eliminates the heavy reliance on dynamic frequency tuning inherent to conventional highly expressive operations, thereby mitigating frequency crowding and crosstalk issues in large-scale quantum processors. We provide a more detailed comparison with conventional schemes in Appendix E. By leveraging engineered transition pathways and auxiliary subspaces, our scheme enables complex conditional operations using experimentally accessible two-qubit gates, with advantages that become increasingly significant for higher-order controlled operations in scalable quantum algorithms.

3 Results

3.1 Controlled rotation and tunable phase

We performed the experimental demonstration on the *Wukong* 72-qubit superconducting quantum platform (see Appendix C for device parameters). First, we carefully calibrated the waveform pulse of the $\sqrt{\mathrm{CZ}}$ component to achieve a full exchange between states $|11\rangle$ and $|20\rangle$, as shown in Figure 2(a). Specifically, we determined the parameters of the coupler and qubits using a peak-finding algorithm and the Nelder-Mead optimization algorithm. We also implemented the derivative reduction by adiabatic gate (DRAG) scheme on the X^{12} gate to minimize leakage and phase errors from other energy levels [54]. We employed error-amplification sequences to precisely optimize the parameters for both single-qubit and two-qubit operations, the details of which are provided in Appendix D.

Next, we conducted a preliminary characterization of the CU operation using the setups depicted in Figures 2(b) and (c). We varied θ in the CU operation and observed the final states with the qubit pair initially prepared in the state $|11\rangle$ to verify the tunable rotation. The results presented in Figure 2(d) show that the population of $|10\rangle$ (P_{10}, red points) varies continuously with θ, following the theoretical prediction $P_{10} = \sin^2(\theta/2)$ (red line). The population of $|11\rangle$ (P_{11}, green points) also remains consistent with the expected $P_{11} = \cos^2(\theta/2)$ (green line). Additionally, the insets in Figure 2(d) show the experimental truth tables of the CPHASE, Controlled Hadamard (CH), and CNOT gates when θ is set to 0, $\pi/2$, and π, respectively.

To evaluate the tunability of the phase ϕ in the CU operation, we measured the controlled phase after applying a CU operation with $\theta = \pi$ while varying ϕ. The qubit pair was initially prepared in the state $|1+\rangle$, and a rotation layer ($\mathrm{X}^{01}_{\pi/2}$) was applied to project the states for measurement, and the results are plotted in Figure 2(e). As a result, P_{10} exhibits sinusoidal oscillations with a period of $T = \pi$ when $\phi' \in [0, 2\pi]$, consistent with the theoretical prediction $P_{10} = \cos^2(\phi')$, where $\phi' = \phi + \phi_0$ incorporates the single-qubit phase ϕ_0. Similarly, the population of $|11\rangle$ (P_{11}) follows the theoretical prediction $P_{11} = \sin^2(\phi')$.

These results demonstrate that our scheme allows for operation selection within a continuous range by simply adjusting the $\mathrm{X}^{12}_{\theta,\phi'}$ gate. The advanced control techniques developed in single-qubit studies ensure the high accuracy

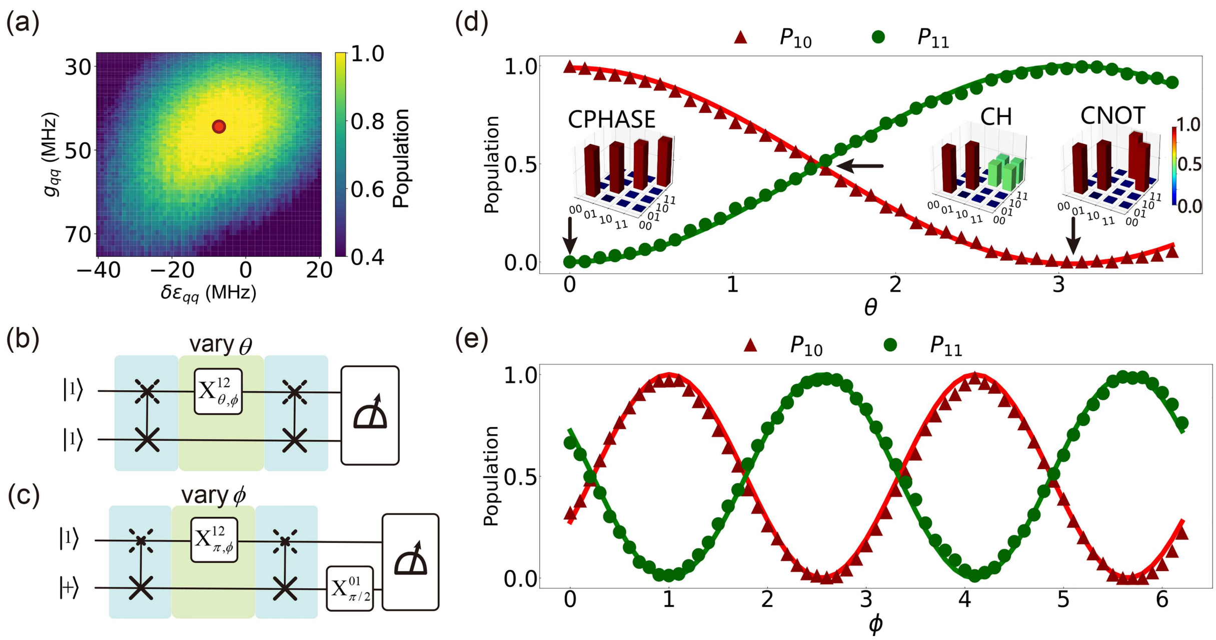

Figure 2 (a) Landscapes of P_{20} as a function of detuning ($\delta\varepsilon_{qq} = \varepsilon_{|11\rangle} - \varepsilon_{|20\rangle}$) and effective coupling strength (g_{qq}). The $\sqrt{\mathrm{CZ}}$ operation time is 30 ns. (b) Schematic setup for verifying the controlled rotation. (c) Schematic setup for verifying the tunable phase. (d) Experimental results corresponding to (b). Dots represent experimental data with 5000 shots, while lines depict theoretical predictions. CPHASE, CH, and CNOT gates can be implemented by setting θ to specific values. Theoretical (gray) and experimental (colored) truth tables for these gates are shown in the insets. (e) Experimental results corresponding to (c). A relative phase offset exists between ϕ and ϕ', originating from the relative phase between X^{12} and X^{01} and the two-qubit interaction. More details and experimental verifications are provided in Appendix I.

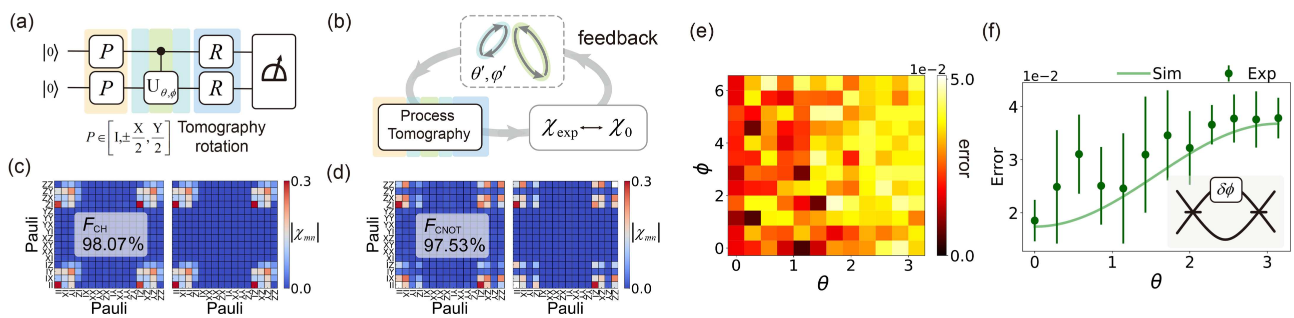

Figure 3 Characterization of the TCG-CU gate. (a) Gate sequences for QPT. (b) Diagram of the optimization protocol incorporating QPT and a feedback mechanism. New parameters are applied to the next pulse based on the comparison between χ_0 and χ_{exp}. Comparison between experimental (left) and theoretical (right) χ matrices for the (c) CH gate and (d) CNOT gate, respectively, incorporating single-qubit phases. (e) Error rates obtained from QPT for the CU family. Each data point represents the average of 10 QPT experiments. Error rates remain below 4.8%, increasing with θ (0–π) while showing no obvious correlation with ϕ (0–2π). (f) Slice experiment results with $\phi = \pi$ at varying θ. Comparison between simulation (line) and experimental results (points), both showing a degradation trend as θ increases. The inset illustrates the leakage cancellation utilizing single-qubit rotation in the process, which is detailed in Appendix F.

and reliability of our CU operation. The ability to switch freely simplifies the physical implementation of highly expressive gates. We further note that our scheme exhibits optimization advantages (Appendix H) as well as enhanced robustness to frequency drift (Appendix G), which stems from reduced sensitivity to controlled phase accumulation.

3.2 Characterization via quantum process tomography

We optimized the fidelities of the CU family using both standard quantum process tomography (QPT) and a feedback-optimized protocol, as depicted in Figures 3(a) and (b), respectively. In this protocol, the experimental quantum process matrices (χ_{exp}) are obtained via QPT, and the fidelities are used as the cost function for the optimization process. Updated X^{12} operations are then applied iteratively until χ_{exp} converges towards the expected process matrix (χ_0). Details are provided in Appendix D. For instance, Figure 3(c) displays the final χ_{exp} and χ_0 for a CNOT gate, where the measured χ_{exp} exhibits the anticipated block structure with a process fidelity of $97.53\% \pm 0.82\%$, determined by $F = \mathrm{Tr}(\chi_{\mathrm{exp}}\chi_0)$. Similarly, Figure 3(d) shows a CH gate achieving a process fidelity

Table 1 Comparison of the number of single-qubit gates (N_{1q}), two-qubit gates (N_{2q}), and circuit depth (d) in entangled state preparation circuits with m qubits ($m \geqslant 3$). The QPU topology must be considered for practical implementation. For simplicity, we only consider unidirectional preparation methods on a one-dimensional qubit chain.

	N_{1q}	N_{2q}	d
GHZ (CZ)	$2m-1$	$m-1$	$2m-1$
W (CZ)	$5m-6$	$3m-5$	$6m-9$
GHZ (CU)	1	$m-1$	m
W (CU)	2	$2m-3$	$2m-1$

of $98.07\% \pm 1.02\%$.

Subsequently, the fidelities of the CU family were determined using the process described above, as presented in Figure 3(e). Experimental results indicate that the process fidelities of these operations range from $96.22\% \pm 0.38\%$ to $98.14\% \pm 0.39\%$. Under identical settings, numerical simulations performed with the QuTiP package yield error rates below 5×10^{-5} [55]. Our simulation analysis thus indicates that decoherence is the dominant source of error. To further analyze the error sources, we conducted a slice experiment with ϕ fixed at π and overlaid this single experimental trace (points) with the corresponding simulation (line) in Figure 3(f). The monotonic decrease in both experimental and simulated fidelities with increasing θ suggests that the X^{12} operation plays a significant role in this degradation. Numerical simulations under decoherence confirm that the $\sqrt{\mathrm{CZ}}$ gate introduces a leakage error corresponding to a 1.126π rotation in the $|11\rangle \leftrightarrow |20\rangle$ subspace. The X^{12} operation disrupts the interference that would otherwise cancel this leakage, causing the leakage population to grow as θ increases [42, 43]. In addition, the intrinsic single-qubit leakage of X^{12} itself becomes more pronounced at higher drive amplitudes due to the broadened pulse spectrum and the resulting spectral overlap with transitions to leakage states [54, 56]. We have included a comprehensive discussion of these error contributions in Appendix F. Finally, these results also encompass errors from initial state preparation and tomography rotations. To mitigate the dominant error channels, practical strategies for leakage and decoherence include integrating Purcell filtering to suppress qubit state decay [57, 58], precisely calibrating and compensating for waveform distortions [50, 59, 60], and employing waveform-shaping techniques such as Fourier-basis waveforms or piecewise-constant-slope waveforms, alongside more fine-grained designs based on machine learning [41, 61–63]. We believe that the concerted application of these techniques will significantly improve the fidelity and robustness of the TCG scheme.

3.3 Entangled-state preparation

Entangled states are fundamental to quantum algorithms, quantum communication, and quantum metrology [64–66]. Notable schemes for preparing entangled states include parallelized circuit scheduling [67–71], variational quantum algorithm (VQA) optimization [72, 73], measurement-assisted protocols [74], and native multi-qubit interactions [65, 75]. However, as the qubit count grows, measurement-based schemes suffer from rapidly increasing rejection rates, while native multi-qubit approaches are limited by the difficulty of achieving fine-grained control. In digital schemes, the corresponding preparation circuits become increasingly complex, and accumulated gate errors and decoherence can substantially reduce the resulting state fidelity. Employing a more expressive gate set can effectively reduce circuit depth in digital schemes, thereby mitigating these detrimental effects.

Compared to conventional CZ-based circuits, our CU-based preparation of three-qubit W and GHZ states achieves circuit depth reductions of 40.0% and 44.0%, respectively. As the qubit number (m) increases, these reductions approach 50.0% and 66.7%, respectively—a detailed comparison is provided in Table 1. We present the preparation circuits for two types of three-qubit entangled states under the TCG scheme as follows:

$$|\Psi_{\mathrm{GHZ}}\rangle = \frac{1}{\sqrt{2}}\left(|000\rangle + e^{i\tau}|111\rangle\right), \tag{5}$$

$$|\Psi_{\mathrm{W}}\rangle = \frac{1}{\sqrt{3}}\left(|001\rangle + \lambda|010\rangle + \sqrt{2-\lambda^2}|100\rangle\right), \tag{6}$$

where $\tau \in [0, 2\pi]$ and $\lambda \in [0, \sqrt{2}]$ correspond to the GHZ and W state families.

We employ optimized TCG-CU and CZ gates, respectively, as entangling operations to generate families of GHZ and W states, and use standard quantum state tomography (QST) to benchmark their performance. Since state preparation involves a unidirectional transition from one quantum state to another, the SPCU gate can be efficiently applied, as illustrated in Figures 4(a) and (b). Detailed circuit schematics are provided in Appendix J. Figure 4(c) shows the corresponding quantum circuits used to prepare entangled states, where the colored operations implement

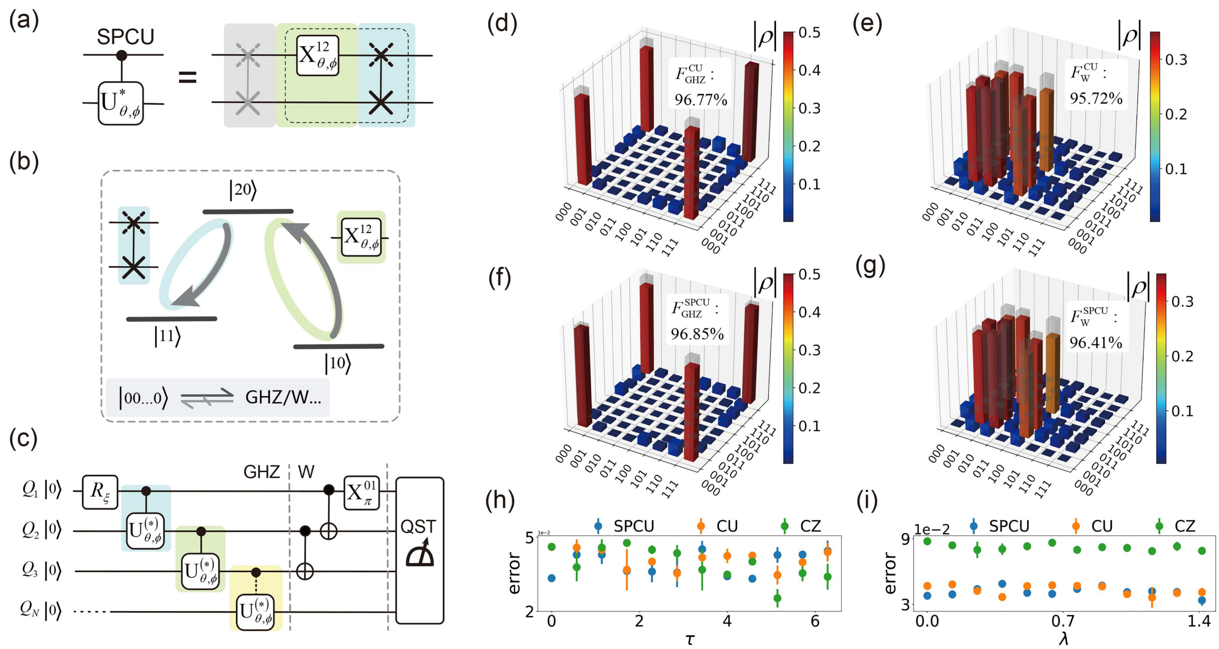

Figure 4 (a) Illustration of the composition of the SPCU gate under the SPTCG scheme. The first $\sqrt{\mathrm{CZ}}$ gate is absent from the CU operation. (b) State evolution diagram corresponding to (a). Unlike the full CU operation, the evolution path of the SPCU is unidirectional. (c) Quantum circuits for preparing and characterizing GHZ and W states. Colored controlled operations in the circuits are implemented using the TCG or SPTCG schemes, while others are realized using the TCG schemes. R_ξ is an SU_2 single-qubit gate composed of two $\mathrm{X}^{01}_{\pi/2}$ gates, treated as a single operation here for consistency. Experimental density matrices ρ of the (d) standard GHZ and (e) W states based on the TCG scheme, respectively, while (f) and (g) are obtained from the SPTCG scheme. Theoretical predictions are marked in gray. (h) Comparison of $F_{|\Psi_{\mathrm{GHZ}}\rangle}$ with different τ constructed using SPCU, CU, and CZ operations. (i) Comparison of $F_{|\Psi_{\mathrm{W}}\rangle}$ with varying λ. Each data point represents the average of 20 QST experiments.

the TCG scheme. The W-preparation circuits require additional controlled and X gates compared to the GHZ-preparation circuits. We then reconstruct the state density matrix (ρ) via QST and calculate the state fidelities using the formula $F = \langle\Psi|\rho|\Psi\rangle$, where $|\Psi\rangle$ is the target state. The QST results for the standard GHZ and W states under CU (SPCU) operations are presented in Figures 4(d)–(g), yielding state fidelities of $96.77\% \pm 0.20\%$ ($96.85\% \pm 0.22\%$) and $95.72\% \pm 0.23\%$ ($96.41\% \pm 0.17\%$), respectively. Furthermore, the fidelities of the states $|\Psi_{\mathrm{GHZ}}\rangle$ and $|\Psi_{\mathrm{W}}\rangle$ are benchmarked in Figures 4(h) and (i), with values ranging from 95.0% to 97.0%. These results also indicate that SPCU-based preparation offers a slight performance advantage over CU-based preparation due to its shallower circuit depth. In preparing states $|\Psi_{\mathrm{GHZ}}\rangle$ and $|\Psi_{\mathrm{W}}\rangle$, our scheme achieves average improvements of 0.35% (from 96.06% to 96.41%) and 4.20% (from 91.72% to 95.92%), respectively, compared to conventional CZ-based circuits. This advantage is expected to become increasingly significant for large-scale entangled state preparation and other complex quantum circuits, where circuit depth reduction becomes more critical.

3.4 Quantum comparator

The quantum comparator, composed of multi-qubit conditional operations, is an essential component in various quantum algorithms, such as Grover's algorithm and quantum sorting algorithms [28–30]. It functions as a quantum decision-making unit, determining the relationship between two quantum states and adjusting the output accordingly. The basic structure of a single-bit quantum comparator is depicted in Figure 5(a). This comparator compares the magnitude of two quantum states $|a\rangle$ and $|b\rangle$ encoded in qubits Q_2 and Q_3, outputting the comparison result to qubits Q_1 and Q_4, as summarized in Table 2. However, traditional quantum comparators based on Clifford decompositions are prone to decoherence and gate error accumulation due to their complex and deep circuit structures.

To address these issues, we construct and demonstrate a four-qubit single-bit quantum comparator using the TCG scheme. As shown in Figure 5(b), the architecture adopts a trapezoidal structure with inherent symmetry, ensuring unitarity. Multiple CU operations are nested to collectively access an auxiliary subspace before coherently returning to $\mathrm{S_c}$. Two additional single-qubit gates are introduced to facilitate state transitions. Compared to the traditional Clifford decomposition, our design achieves significant optimization, reducing circuit complexity and depth to approximately 41.2% and 28.0% of the standard values, respectively, as detailed in Table 3.

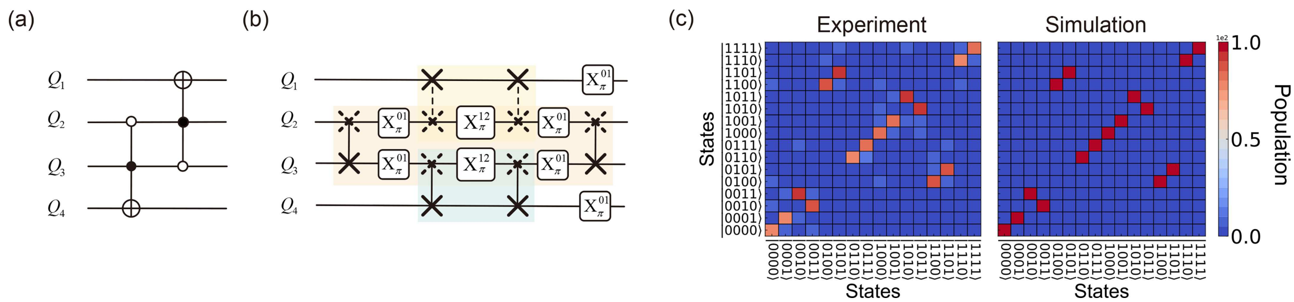

Figure 5 (a) Equivalent circuit of a single-bit quantum comparator, constructed using two multi-controlled gates. (b) Detailed implementation of the quantum comparator under the TCG scheme, comprising multiple nested CU gates distinguished by different colors. (c) Comparison of the experimental and theoretical truth tables for the quantum comparator, with each data point derived from 5000 measurement shots.

Table 2 Function of the quantum comparator. The first column ('Condition') lists the specific comparison conditions between the two input states. It compares the quantum states of qubits Q_2 ($|a\rangle$) and Q_3 ($|b\rangle$). Based on this comparison, the result is encoded in the states of qubits Q_1 and Q_4 (initialized to $|00\rangle$).

Condition	Q_2 ($\|a\rangle$)	Q_3 ($\|b\rangle$)	Q_1	Q_4
$a = b$	$\|0\rangle$	$\|0\rangle$	$\|0\rangle$	$\|0\rangle$
$a = b$	$\|1\rangle$	$\|1\rangle$	$\|0\rangle$	$\|0\rangle$
$a > b$	$\|1\rangle$	$\|0\rangle$	$\|1\rangle$	$\|0\rangle$
$a < b$	$\|0\rangle$	$\|1\rangle$	$\|0\rangle$	$\|1\rangle$

Table 3 Comparison of the number of single-qubit gates (N_{1q}), two-qubit gates (N_{2q}), and circuit depth (d) in quantum comparator construction. In practical Clifford-based schemes, the actual gate complexity often exceeds the values shown here due to the additional overhead from decomposing nonlocal controlled gates.

	N_{1q}	N_{2q}	d
Clifford	22	12	25
TCG	8	6	7

Experimentally, we compared the theoretical (M_0) and experimental (M_e) results of the comparator truth table (Figure 5(c)) and observed excellent agreement. The achieved fidelity was approximately $71.06\% \pm 2.4\%$, calculated using the following formula:

$$F = \left(\mathrm{Tr}\left(M_e^\dagger M_e\right) + \left|\mathrm{Tr}\left(M_0^\dagger M_e\right)\right|^2 \right) / \left(d(d+1)\right), \tag{7}$$

where $d = 16$. In contrast, attempts to construct comparators using CZ gates failed due to noise accumulation and errors in the deeper circuits. These results highlight the robustness and scalability of our scheme, demonstrating its clear advantages and potential for constructing complex quantum circuits.

4 Discussion and conclusion

In summary, we proposed the TCG scheme and experimentally demonstrated the TCG-CU gate and its applications on a superconducting transmon platform, which offers convenient control and reduced complexity. Our scheme leverages high-energy levels as auxiliary states instead of auxiliary qubits, enabling independent control freedom via internal operations and transition conversions. These highly expressive and easily manipulated operations serve as key components for significantly reducing quantum circuit depth, thereby mitigating decoherence effects and gate error accumulation, providing a hardware-efficient foundation for implementing complex near-term algorithms, such as those used in portfolio optimization and computational insurance [76, 77]. Furthermore, the short-path TCG (SPTCG) scheme can further lower the complexity of various quantum circuits, such as state preparation circuits, making it highly suitable for large-scale quantum communications and simulations.

The sandwich-like CU gate was implemented and optimized using the QPT method with a feedback loop, while detailed slice analysis indicates that decoherence and leakage remain the dominant error sources. In three-qubit entangled-state preparation, CU-based circuits reduce the circuit depth for GHZ and W states by 40.0% and 44.0%, respectively, compared to conventional CZ-based implementations. For larger systems, these reductions scale to nearly 50.0% and 66.7%, respectively. Furthermore, we experimentally demonstrated a quantum comparator with a fidelity of 71.06% and a 72.00% reduction in circuit depth. These results highlight the significant potential of our scheme for optimizing quantum circuits, particularly in the NISQ era where circuit depth minimization is essential for suppressing error accumulation.

We also note that the transient occupation of high-energy levels within the non-uniform energy level structure provides additional degrees of freedom for gate construction, enabling the realization of more complex controlled operations [78–80]. However, further exploration of model-based approaches is necessary to move beyond manually constructed designs and achieve arbitrary gate implementations. Quantum signal processing (QSP) introduces a parameterized approach for designing quantum operations, providing a promising avenue in this regard [81, 82]. Meanwhile, increased control errors and decoherence at high-energy levels may degrade the operational fidelity of the TCG scheme. To fully unlock its potential, advanced qubit design strategies and waveform optimization techniques will be essential to mitigate these challenges and enhance performance [48, 61, 83].

Acknowledgements This work was supported by National Key Research and Development Program of China (Grant No. 2023YFB4502500) and National Natural Science Foundation of China (Grant No. 12404564). This work was partially carried out at the USTC Center for Micro and Nanoscale Research and Fabrication.

Supporting information Appendixes A–J. The supporting information is available online at info.scichina.com and link.springer.com. The supporting materials are published as submitted, without typesetting or editing. The responsibility for scientific accuracy and content remains entirely with the authors.

References

1 Preskill J. Quantum computing in the NISQ era and beyond. Quantum, 2018, 2: 79

2 Kjaergaard M, Schwartz M E, Braumüller J, et al. Superconducting qubits: current state of play. Annu Rev Condens Matter Phys, 2020, 11: 369–395

3 Arute F, Arya K, Babbush R, et al. Quantum supremacy using a programmable superconducting processor. Nature, 2019, 574: 505–510

4 Gao D, Fan D, Zha C, et al. Establishing a new benchmark in quantum computational advantage with 105-qubit Zuchongzhi 3.0 processor. Phys Rev Lett, 2025, 134: 090601

5 Fowler A G, Mariantoni M, Martinis J M, et al. Surface codes: towards practical large-scale quantum computation. Phys Rev A, 2012, 86: 032324

6 Gonzalez-Raya T, Asensio-Perea R, Martin A, et al. Digital-analog quantum simulations using the cross-resonance effect. PRX Quantum, 2021, 2: 020328

7 Sim S, Johnson P D, Aspuru-Guzik A. Expressibility and entangling capability of parameterized quantum circuits for hybrid quantum-classical algorithms. Adv Quantum Tech, 2019, 2: 1900070

8 Peterson E C, Crooks G E, Smith R S. Two-qubit circuit depth and the monodromy polytope. Quantum, 2020, 4: 247

9 Abrams D M, Didier N, Johnson B R, et al. Implementation of XY entangling gates with a single calibrated pulse. Nat Electron, 2020, 3: 744–750

10 Roy T, Hazra S, Kundu S, et al. Programmable superconducting processor with native three-qubit gates. Phys Rev Appl, 2020, 14: 014072

11 Kim Y, Morvan A, Nguyen L B, et al. High-fidelity three-qubit iToffoli gate for fixed-frequency superconducting qubits. Nat Phys, 2022, 18: 783–788

12 Glaser N J, Roy F, Filipp S. Controlled-controlled-phase gates for superconducting qubits mediated by a shared tunable coupler. Phys Rev Appl, 2023, 19: 044001

13 Chen Z, Liu W, Ma Y, et al. Efficient implementation of arbitrary two-qubit gates via unified control, 2025. ArXiv:2502.03612

14 Caldwell S A, Didier N, Ryan C A, et al. Parametrically activated entangling gates using transmon qubits. Phys Rev Appl, 2018, 10: 034050

15 Hong S S, Papageorge A T, Sivarajah P, et al. Demonstration of a parametrically activated entangling gate protected from flux noise. Phys Rev A, 2020, 101: 012302

16 Sete E A, Didier N, Chen A Q, et al. Parametric-resonance entangling gates with a tunable coupler. Phys Rev Appl, 2021, 16: 024050

17 Foxen B, Neill C, Dunsworth A, et al. Demonstrating a continuous set of two-qubit gates for near-term quantum algorithms. Phys Rev Lett, 2020, 125: 120504

18 Brink M, Chow J M, Hertzberg J, et al. Device challenges for near term superconducting quantum processors: frequency collisions. In: Proceedings of 2018 IEEE International Electron Devices Meeting (IEDM), 2018

19 Osman A, Fernández-Pendás J, Warren C, et al. Mitigation of frequency collisions in superconducting quantum processors. Phys Rev Res, 2023, 5: 043001

20 Morvan A, Chen L, Larson J M, et al. Optimizing frequency allocation for fixed-frequency superconducting quantum processors. Phys Rev Res, 2022, 4: 023079

21 Yang T, Wang W, Wang L, et al. A superconducting quantum processor architecture design method for improving performance and reducing frequency collisions. Results Phys, 2023, 53: 106944

22 Wan L C, Yu C H, Pan S J, et al. Block-encoding-based quantum algorithm for linear systems with displacement structures. Phys Rev A, 2021, 104: 062414

23 Sünderhauf C, Campbell E, Camps J. Block-encoding structured matrices for data input in quantum computing. Quantum, 2024, 8: 1226

24 Kane C F, Hariprakash S, Modi N S, et al. Block encoding bosons by signal processing. Quantum, 2025, 9: 1747

25 Pedersen L H, Møller N M, Mølmer K. Fidelity of quantum operations. Phys Lett A, 2007, 367: 47–51

26 Bialczak R C, Ansmann M, Hofheinz M, et al. Quantum process tomography of a universal entangling gate implemented with Josephson phase qubits. Nat Phys, 2010, 6: 409–413

27 Magesan E, Blume-Kohout R, Emerson J. Gate fidelity fluctuations and quantum process invariants. Phys Rev A, 2011, 84: 012309

28 Oliveira D S, Ramos R V. Quantum bit string comparator: circuits and applications. Opt Quant Electron, 2007, 7: 17–26

29 Xia H, Li H, Zhang H, et al. An efficient design of reversible multi-bit quantum comparator via only a single ancillary bit. Int J Theor Phys, 2018, 57: 3727–3744

30 Xia H, Li H, Zhang H, et al. Novel multi-bit quantum comparators and their application in image binarization. Quantum Inf Process, 2019, 18: 1–7

31 Krantz P, Kjaergaard M, Yan F, et al. A quantum engineer's guide to superconducting qubits. Appl Phys Rev, 2019, 6: 021318

32 Koch J, Yu T M, Gambetta J, et al. Charge-insensitive qubit design derived from the Cooper pair box. Phys Rev A, 2007, 76: 042319

33 Barends R, Kelly J, Megrant A, et al. Coherent Josephson qubit suitable for scalable quantum integrated circuits. Phys Rev Lett, 2013, 111: 080502

34 Chen Z, Kelly J, Quintana C, et al. Measuring and suppressing quantum state leakage in a superconducting qubit. Phys Rev Lett, 2016, 116: 020501

35 Barends R, Quintana C M, Petukhov A G, et al. Diabatic gates for frequency-tunable superconducting qubits. Phys Rev Lett, 2019, 123: 210501

36 Hyyppä E, Vepsäläinen A, Papic M, et al. Reducing leakage of single-qubit gates for superconducting quantum processors using analytical control pulse envelopes. PRX Quantum, 2024, 5: 030353

37 Majumdar R, Basu S, Ghosh S, et al. Quantum error-correcting code for ternary logic. Phys Rev A, 2018, 97: 052302

38 Klimov A B, Guzmán R, Retamal J C, et al. Qutrit quantum computer with trapped ions. Phys Rev A, 2003, 67: 062313

39 Goss N, Morvan A, Marinelli B, et al. High-fidelity qutrit entangling gates for superconducting circuits. Nat Commun, 2022, 13: 7481

40 Bækkegaard T, Kristensen L B, Loft N J S, et al. Realization of efficient quantum gates with a superconducting qubit-qutrit circuit. Sci Rep, 2019, 9: 13389

41 Li S, Clark J, Wang S, et al. Realisation of high-fidelity nonadiabatic CZ gates with superconducting qubits. npj Quantum Inf, 2019, 5: 84

42 Rol M A, Battistel F, Malinowski F K, et al. Fast, high-fidelity conditional-phase gate exploiting leakage interference in weakly anharmonic superconducting qubits. Phys Rev Lett, 2019, 123: 120502

43 Negîrneac V, Ali H, Muthusubramanian N, et al. High-fidelity controlled-z gate with maximal intermediate leakage operating at the speed limit in a superconducting quantum processor. Phys Rev Lett, 2021, 126: 220502

44 Chu J, He X, Zhou Y, et al. Scalable algorithm simplification using quantum AND logic. Nat Phys, 2023, 19: 126–131

45 Wang Z, Bao Z, Wu Y, et al. Improved superconducting qubit state readout by path interference. Chin Phys Lett, 2021, 38: 110303

46 Chen L, Li H X, Lu Y, et al. Transmon qubit readout fidelity at the threshold for quantum error correction without a quantum-limited amplifier. npj Quantum Inf, 2023, 9: 26

47 Morvan A, Ramasesh V V, Blok M S, et al. Qutrit randomized benchmarking. Phys Rev Lett, 2021, 126: 210504

48 Chen Y, Duan P, Jia Z L, et al. Distinguishing the impact of oxidation on the Josephson junction oxide barrier through the 1/f behavior. Appl Phys Lett, 2024, 125: 094001

49 Guo L L, Duan P, Du L, et al. Correction of microwave pulse reflection by digital filters in superconducting quantum circuits. Chin Phys B, 2024, 33: 090303

50 Guo L L, Duan P, Zhang S, et al. Universal scalable characterization and correction of pulse distortions in controlled quantum systems. Phys Rev Appl, 2024, 21: 064060

51 Tănăsescu A, Constantinescu D, Popescu P G. Distribution of controlled unitary quantum gates towards factoring large numbers on today's small-register devices. Sci Rep, 2022, 12: 21310

52 Bland M P, Bahrami F, Martinez J G C, et al. 2d transmons with lifetimes and coherence times exceeding 1 millisecond, 2025. ArXiv:2503.14798

53 Tuokkola M, Sunada Y, Kivijärvi H, et al. Methods to achieve near-millisecond energy relaxation and dephasing times for a superconducting transmon qubit. Nat Commun, 2025, 16: 5421

54 Motzoi F, Gambetta J M, Rebentrost P, et al. Simple pulses for elimination of leakage in weakly nonlinear qubits. Phys Rev Lett, 2009, 103: 110501

55 Johansson J R, Nation P D, Nori F. QuTiP: an open-source Python framework for the dynamics of open quantum systems. Comput Phys Commun, 2012, 183: 1760–1772

56 Gambetta J M, Motzoi F, Merkel S T, et al. Analytic control methods for high-fidelity unitary operations in a weakly nonlinear oscillator. Phys Rev A, 2011, 83: 012308

57 Sete E A, Martinis J M, Korotkov A N. Quantum theory of a bandpass Purcell filter for qubit readout. Phys Rev A, 2015, 92: 012325

58 Sunada Y, Kono S, Ilves J, et al. Fast readout and reset of a superconducting qubit coupled to a resonator with an intrinsic Purcell filter. Phys Rev Appl, 2022, 17: 044016

59 Aggarwal A, Fernández-Pendás J, Abad T, et al. Mitigating transients in flux-control signals in a superconducting quantum processor, 2025. ArXiv:2503.08645
60 Li T M, Zhang J C, Chen B J, et al. High-precision pulse calibration of tunable couplers for high-fidelity two-qubit gates in superconducting quantum processors. Phys Rev Appl, 2025, 23: 024059
61 Glaser N J, Roy F A, Tsitsilin I, et al. Closed-loop optimization for high-fidelity controlled-z gates in superconducting qubits. Phys Rev Appl, 2025, 24: 024048
62 Petruhanov V N, Pechen A N. GRAPE optimization for open quantum systems with time-dependent decoherence rates driven by coherent and incoherent controls. J Phys A-Math Theor, 2023, 56: 305303
63 Sarma B, Hartmann M J. Designing fast quantum gates using optimal control with a reinforcement-learning ansatz. Phys Rev Appl, 2025, 23: 014015
64 Horodecki R, Horodecki P, Horodecki M, et al. Quantum entanglement. Rev Mod Phys, 2009, 81: 865–942
65 Song C, Xu K, Li H, et al. Generation of multicomponent atomic Schrödinger cat states of up to 20 qubits. Science, 2019, 365: 574–577
66 Cao S, Wu B, Chen F, et al. Generation of genuine entanglement up to 51 superconducting qubits. Nature, 2023, 619: 738–742
67 DiCarlo L, Reed M D, Sun L, et al. Preparation and measurement of three-qubit entanglement in a superconducting circuit. Nature, 2010, 467: 574–578
68 Mooney G J, White G A L, Hill C D, et al. Generation and verification of 27-qubit Greenberger-Horne-Zeilinger states in a superconducting quantum computer. J Phys Commun, 2021, 5: 095004
69 Bao Z, Xu S, Song Z, et al. Creating and controlling global Greenberger-Horne-Zeilinger entanglement on quantum processors. Nat Commun, 2024, 15: 8823
70 Chen K C. Short-depth circuits and error mitigation for large-scale GHZ-state preparation, and benchmarking on IBM's 127-qubit system. In: Proceedings of 2023 IEEE International Conference on Quantum Computing and Engineering (QCE), 2023. 207–210
71 Javadi-Abhari A, Martiel S, Seif A, et al. Big cats: entanglement in 120 qubits and beyond, 2025. ArXiv:2510.09520
72 Hai V T, Viet N T, Ho L B. Variational preparation of entangled states on quantum computers. 2023. ArXiv:2306.17422
73 áron Rozgonyi, Széchenyi G, Kálmán O, et al. Training iterated protocols for distillation of GHz states with variational quantum algorithms. Phys Lett A, 2024, 499: 129349
74 Hashim A, Yuan M, Gokhale P, et al. Efficient generation of multi-partite entanglement between non-local superconducting qubits using classical feedback. 2025. ArXiv:2403.18768
75 Song C, Xu K, Liu W, et al. 10-qubit entanglement and parallel logic operations with a superconducting circuit. Phys Rev Lett, 2017, 119: 180511
76 Liu H Y, Zhuang X N, Wang C, et al. Quantum computational insurance and actuarial science. Sci China Inf Sci, 2025, 68: 202501
77 Wang S B, Wang P, Li G H, et al. Variational quantum eigensolver with linear depth problem-inspired ansatz for solving portfolio optimization in finance. Sci China Inf Sci, 2025, 68: 180504
78 Blok M S, Ramasesh V V, Schuster T, et al. Quantum information scrambling on a superconducting qutrit processor. Phys Rev X, 2021, 11: 021010
79 Goss N, Ferracin S, Hashim A, et al. Extending the computational reach of a superconducting qutrit processor. npj Quantum Inf, 2024, 10: 101
80 Roy T, Li Z, Kapit E, et al. Two-qutrit quantum algorithms on a programmable superconducting processor. Phys Rev Appl, 2023, 19: 064024
81 Motlagh D, Wiebe N. Generalized quantum signal processing. PRX Quantum, 2024, 5: 020368
82 Dong Y, Lin L, Ni H, et al. Infinite quantum signal processing. Quantum, 2024, 8: 1558
83 Chiaro B, Zhang Y. Active leakage cancellation in single qubit gates. 2025. ArXiv:2503.14731